PHYSICAL REVIEW C VOLUME 19, NUMBER 6 JUNE 1979

Fusion and peripheral reactions of $^{12}C + ^{14}N$ at energies up to 13 MeV/A

J. Gomez del Campo, R. G. Stokstad, J. A. Biggerstaff, R. A. Dayras,* A. H. Snell, and P. H. Stelson
Oak Ridge National Laboratory, Oak Ridge, Tennessee 37830

(Received 20 February 1979)

Angular and energy distributions have been measured for reaction products of the $^{14}N + ^{12}C$ system at nine bombarding energies in the energy range $E_{^{14}N} = 34.1$ to 178.1 MeV. The fusion and direct reaction components for products from Li to Al have been determined. The experimental fusion cross sections and deduced critical angular momenta are discussed in terms of entrance channel models for compound nucleus formation and the rotating liquid drop model. Hauser-Feshbach calculations of the Z distributions, energies, and angular distributions of evaporation residues are presented and compared to the data. The direct reaction yield has been analyzed with a diffraction model and is also compared with time-dependent Hartree-Fock calculations. The experimental total reaction cross section is in good agreement with optical model calculations.

[NUCLEAR REACTIONS $^{14}N+^{12}C$, $E_{^{14}N}=34.1$ to 178.1 MeV, measured $d^2\sigma/d\Omega dE$ for reaction products from $Z=3$ to 13. Extracted σ_{fusion}, σ_{direct}, and σ_{total}.]

I. INTRODUCTION

The measurement of cross sections for fusion and for direct reactions of heavy ions in the mass range $A \sim 10-20$ is of interest in that the division of the cross section among these competing mechanisms is determined by a delicate balance of the nuclear and centrifugal forces acting in a peripheral collision. At high bombarding energies, the effects of Coulomb forces are relatively small, and one has the opportunity to study the dominant effect of angular momentum on compound-nucleus formation.

Considerable effort has been given to the study of the $^{14}N+^{12}C$ system through measurements of the cross section for primary emission of particles such as deuterons,[1] α particles,[1,2] ^{6,7}Li ions,[1,3,4] and ^{7,9}Be ions.[3,4] A review of such measurements is given in Ref. 5. The major emphasis of these studies has been on the reaction mechanism and on the extraction of the critical angular momentum (J_c) for compound-nucleus formation.[5] However, in a recent analysis of the total yields of ^{6,7}Li and ^{7,9}Be (Ref. 4), it has been shown that for $E_{\text{c.m.}} \geq 30$ MeV the method of extracting J_c from primary emission of evaporated particles becomes difficult because of the presence of strong non-compound-nucleus components in the cross section. On the other hand, a measurement of the fusion cross section (σ_{fus}), and therefore of J_c, can be obtained by direct observation of the evaporation residues. Such a measurement of J_c is independent of statistical-model calculations of absolute cross sections.

The measurement of σ_{fus} by observation of the evaporation residues is a technique routinely used for heavier systems,[6] $A_1+A_2 \geq 40$, where the mass or charge of the residue is sufficient to separate it from other products. However, for lighter systems,[7-10] $A_1+A_2 \leq 30$, the separation of the products of direct inelastic reactions from those of fusion becomes more involved when the evaporation residues have masses comparable to or less than that of the projectile. A brief description of our fusion cross section measurements and analyses of the $^{14}N+^{12}C$ system has been given previously.[7] We showed there that the fusion component in the energy spectrum of a given element can be identified by simple kinematic arguments. The extracted energy and angular distributions as well as the relative yields of the evaporation residues were then found to be consistent with statistical-model calculations.[7,11,12] The measurements and analyses of the fusion cross section have been extended up to $E_{^{14}N} = 248$ MeV (Ref. 12) using the methods described in Ref. 7. A maximum value of $27\hbar$ for the critical angular momentum J_c has been observed. This value agrees with the prediction of the rotating liquid-drop model.[13]

In this article we present a complete description of the data and analyses given in Ref. 7, and, in addition, describe the analyses of the direct-reaction components and the elastic scattering. The experimental procedure and results are described in Secs. II and III, respectively. Section IV presents a kinematical analysis of the evaporation residues. A Hauser-Feshbach Monte Carlo calculation and comparison to the data are given in Sec. V. The direct-reaction yield is considered in Sec. VI and the total reaction cross sections in Sec. VII. The conclusions are given in the last section.

II. EXPERIMENTAL PROCEDURE

Energy-analyzed beams of ^{14}N extracted from the Oak Ridge Isochronous Cyclotron were used to bombard natural carbon foils at nine energies covering the range from 34.1 to 178.1 MeV. The thickness of the targets (156 μg/cm^2 and 257 μg/cm^2) was determined both by weighing the foils and by Rutherford scattering of ^{14}N ions at 19 MeV. The results of these two measurements had uncertainties of ± 4% and ± 6%, respectively, and were in good agreement. The principal contaminants in the target were ^{13}C(1%), ^{16}O(1.3%), and hydrogen ($\leq$ 2%).

Reaction products with $Z = 3$ to 13 were detected using ΔE-E counter telescopes. One of the detection systems was a position-sensitive ΔE-E telescope[14] which was used to measure nine angles simultaneously. The other detector was a narrowly collimated ΔE-E telescope used mainly to observe particles at small scattering angles (~4°–8°). In both cases, the ΔE element was an ionization chamber. Angular distributions were measured for the range of laboratory angles from 4° to 40°. The absolute normalization for the cross section was derived from the target thickness, detector solid angle, and integrated beam currents. The error on the fusion cross sections varied from ± 8% to ± 12%, depending on the bombarding energy.

III. RESULTS

Figure 1 shows a typical two-dimensional E-ΔE spectrum measured at $E_{^{14}\mathrm{N}} = 43.9$ MeV and a laboratory angle of 10°. The lines drawn around each group identify the different elements. Figure 2 shows another spectrum taken at a laboratory energy $E_{^{14}\mathrm{N}} = 178.1$ MeV and $\theta_{\mathrm{lab}} = 6°$. Note the increased yield of lighter elements at the higher bombarding energy.

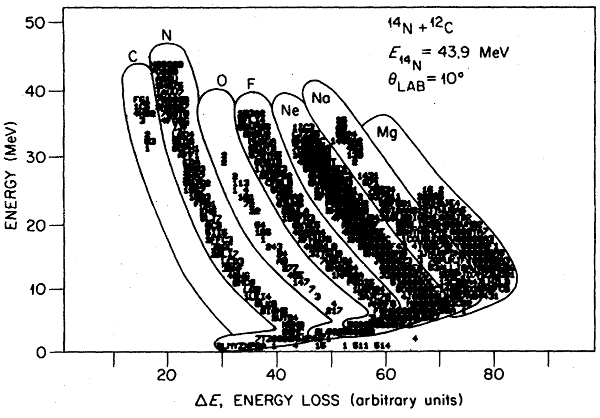

FIG. 1. ΔE vs E array for the reaction products of ^{14}N+^{12}C at $E_{^{14}\mathrm{N}}=43.9$ MeV and $\theta_{\mathrm{lab}}=10°$. The total energy E was obtained by analog summation of the signals from the ionization chamber and solid-state detector. The curves around the contours of constant Z are used to obtain projections along the E axis.

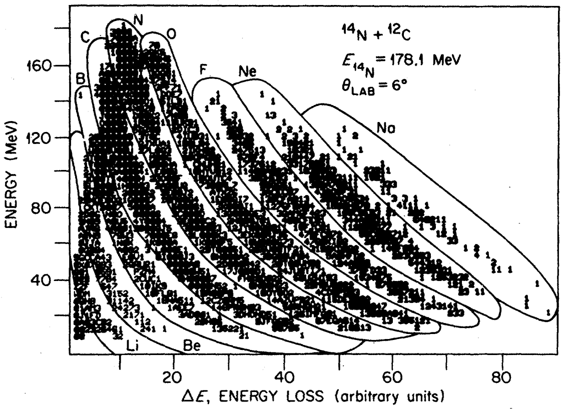

FIG. 2. ΔE vs E array for the reaction products of ^{14}N+^{12}C at $E_{^{14}\mathrm{N}}=178.1$ MeV and $\theta_{\mathrm{lab}}=6°$. Note the increased yield for lighter elements relative to the data shown in Fig. 1. The solid lines have the same meaning as in Fig. 1.

From the two-dimensional spectra such as those shown in Figs. 1 and 2, the energy distributions ($d^2\sigma/d\Omega dE$) and the energy-integrated angular distributions for evaporation residues ($d\sigma/d\Omega$ or $d\sigma/d\theta$) were extracted for each atomic number for the nine bombarding energies measured. Typical examples of these distributions are shown in Figs. 3 and 4 for ^{14}N energies of 53.2 and 145.5 MeV, respectively. The energy spectra such as those shown on the right-hand sides of Figs. 3 and 4 exhibit the basic features of the reaction mechanism and can be understood by simple kinematic arguments. For example, the energy spectra for Mg, Na, and Ne shown in Fig. 3 have the characteristics of evaporation residues: The centroids of the distributions occur at an energy corresponding to a velocity approximately equal to that of the compound nucleus. The spectrum for Ne ions shows two strong groups that arise from the forward and backward center-of-mass emission of an α particle and a proton. Similar structures have been seen in measurements of the residues of ^{12}C+^{16}O (Ref. 8).

The energy spectra for oxygen, nitrogen, and carbon ions shown in Fig. 4 exhibit, in addition to the lower-energy group characteristic of evaporation residues, a component at higher energy whose velocity is typical of that of the projectile. These higher-energy components arise from direct two-body reactions in which one or more nucleons are either transferred or are emitted by the projectile after having been excited in a peripheral collision. The dashed lines drawn in Fig. 4 for the low- and high-energy components of carbon ions indicate

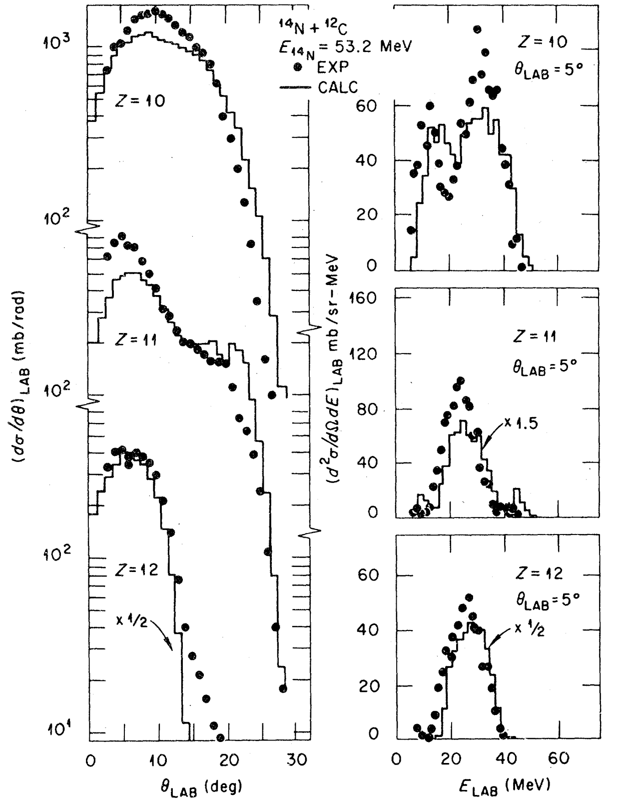

FIG. 3. Energy and angular distributions for reaction products from Ne to Mg in the $^{14}N + ^{12}C$ system at $E_{^{14}N} = 53.2$ MeV. The left side shows the angular distributions in a $(d\sigma/d\theta)_{lab}$ vs θ_{lab} plot. The double structure seen in the angular distribution for $Z = 11$ corresponds to the emission of $2p$ or $2pn$ (forward peaked) and α or αn (at larger angles). The energy distributions shown on the right side for $\theta_{lab} = 5°$ display the characteristic features of evaporation residues. The histograms are the results of the Monte Carlo Hauser-Feshbach calculations discussed in the text.

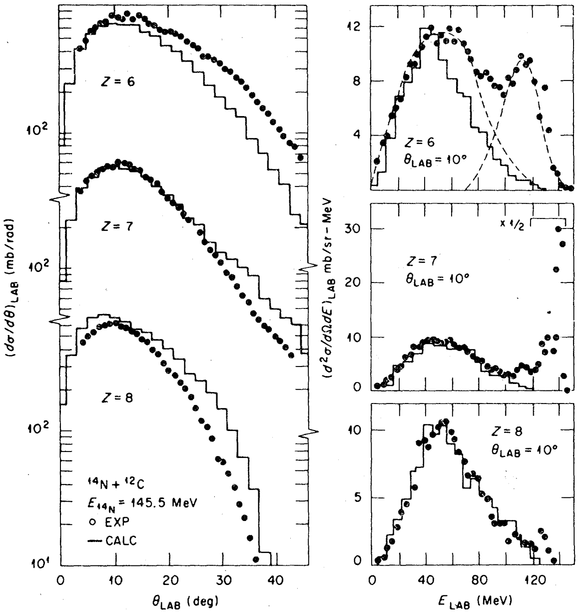

FIG. 4. Energy and angular distributions for reaction products from O to C for the $^{14}N + ^{12}C$ reaction at $E_{14\,N} = 145.5$ MeV. The energy distributions for carbon ions, plotted on the right side, show components characteristic of evaporation residues (the lower-energy component) and of direct reactions (the higher-energy component). The dashed lines indicate the way these two components were unfolded. The histograms have the same meaning as in Fig. 3.

the manner in which the evaporation-residue and direct-reaction components were unfolded. The angular distributions for the lower-energy (fusion) components for $Z = 6$, 7, and 8 are shown on the left side of Fig. 4. The angular distributions of a direct-reaction product and an evaporation residue, e.g., for $Z = 6$, are quite different, with the former distribution being more strongly forward peaked. This is illustrated in Figs. 5 and 6, which show angular distributions for the evaporation residues and direct-reaction components produced at $E_{^{14}N} = 145.5$ MeV. Note in each of the cases shown in Figs. 3, 4, and 5 how the angular distribution for evaporation residues is shifted toward larger angles as more mass is evaporated. Figure 6 shows the rapid decrease with increasing scattering angle of the differential cross section for direct-reaction products. A quantitative discussion of these kinematic considerations will be given in subsequent sections. An important point for the present analysis is that the direct-reaction and evaporation-residue components in the energy spectra have been unfolded in a systematic manner (see Fig. 4) using the structure present in the spectrum itself as a guide. Thus, the deduction of the absolute cross sections is essentially independent of a statistical-model calculation. Confidence in this procedure for unfolding the spectra is provided by the fact that it then yields angular distributions for the separate components which are in general agreement with predictions of models incorporating the essential reaction mechanisms of compound-nucleus and direct-reaction processes.

The fusion cross section was extracted for each of the nine bombarding energies from 34.1 to 178.1 MeV by integration of the angular distributions for the evaporation residues. Typical examples of such distributions are shown for $E_{^{14}N} = 145.5$ MeV in Fig. 5 for residues from sodium to boron. No residues were observed for Mg or Al. The solid lines drawn through the data points indicate the trend of the data and were used to extrapolate the cross sections outside the angular range of the measurements. For large angles

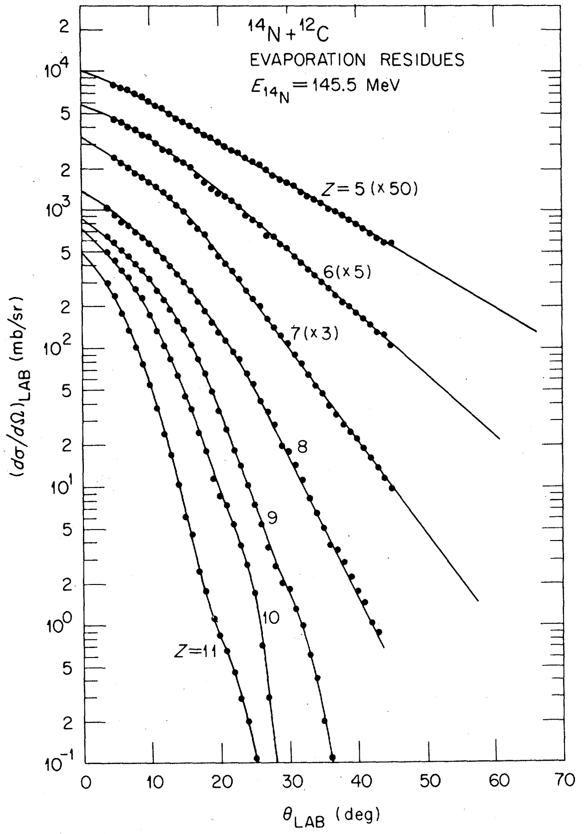

FIG. 5. Angular distributions for the evaporation residue products of the fusion of $^{14}N+^{12}C$ at $E_{^{14}N}=145.5$ MeV. The solid lines drawn through the data points indicate the way the cross section was extrapolated toward unmeasured angles. The total amount of extrapolation is less than 6% of the fusion cross section.

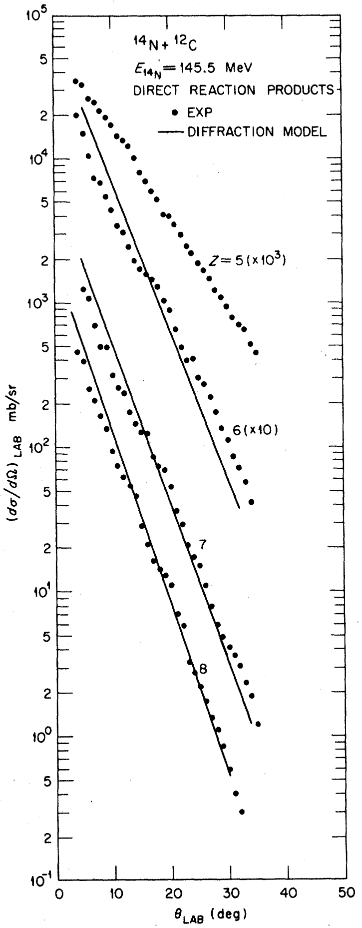

FIG. 6. Angular distribution for the direct-reaction components of the $^{14}N+^{12}C$ system at $E_{^{14}N}=145.5$ MeV. The solid lines drawn through the data points are the results of a diffraction-model calculation discussed in the text.

these lines were terminated at a value of θ_{max} estimated with Eq. (6) (see Sec. IV). The integration of the angular distributions of Fig. 5 yields a value of $\sigma_{fus}=980$ mb of which only 6% comes from this extrapolation. This amount of extrapolated cross section was typical for all the fusion measurements. Contributions from the low-energy recoiling partner produced in direct peripheral reactions (see Sec. VI) are negligible.

Table I shows the results for the fusion cross

TABLE I. Fusion cross sections and critical angular momenta for the $^{14}N+^{12}C$ system.

E_{lab} (MeV)	$E_{c.m.}$ (MeV)	E_x (MeV)	σ_{fus} (mb)	$J_c(\hbar)$
34.1	15.7	30.8	945 ± 75	11.1 ± 0.50
43.9	20.3	35.3	967 ± 75	12.9 ± 0.50
53.2	24.6	39.6	964 ± 75	14.3 ± 0.56
60.0	27.7	42.8	932 ± 75	15.0 ± 0.60
86.3	39.8	54.9	895 ± 80	17.8 ± 0.80
106.3	49.1	64.1	913 ± 80	20.0 ± 0.90
145.5	67.2	82.2	1005 ± 80	24.8 ± 1.0
158.0 [a]	72.9	88.0	987 ± 80	25.7 ± 1.0
167.1	77.1	92.2	888 ± 85	25.0 ± 1.2
178.1	82.2	97.3	932 ± 85	26.5 ± 1.2
248.0 [a]	114.5	129.6	717 ± 85	27.5 ± 1.7

[a] Values from Ref. 12.

sections for the nine bombarding energies. Columns 1 and 2 give the laboratory bombarding energy E_{lab} and center-of-mass energy $E_{\text{c.m.}}$, respectively. The excitation energy E_x in the compound system is given in column 3, while column 4 shows the fusion cross section (mb). The errors contain contributions from uncertainties in the target thickness, solid angle, and beam current integration and also from uncertainties in the unfolding of the energy spectra (of consequence only for residues $Z \leqslant 7$). The values of σ_{fus} for $E_{^{14}\text{N}} \geqslant 145$ MeV have been increased by small amounts corresponding to estimates of the yields of residues with $Z < 5$. As disussed in Sec. VI, the production of Li and Be can originate with several mechanisms. It was not possible using the methods to be described in Secs. III and IV to identify the Li and Be evaporation-residue components, and hence the estimation of these residues was done using the statistical-model calculations. These estimates are 2%, 5%, and 7% of σ_{fus} for the bombarding energies of 145.5, 167.1, and 178.1 MeV, respectively.

The relationship between the fusion cross section and the transmission coefficients T_l, describing the probability of compound-nucleus formation for a partial wave l and total angular momentum J, is

$$\sigma_{\text{fus}} = \frac{\pi \lambdabar^2}{(2I+1)(2i+1)} \sum_{J=0,\, l=|J-S|}^{J_c,\, J+S} (2l+1)T_l\,, \qquad (1)$$

where i and I are the projectile and target spins, respectively, and the channel spin is given $\vec{s} = \vec{I} + \vec{i}$. For small partial waves $T_l \to 1$, whereas for l values somewhat less than the grazing l value for direct reactions $T_l \to 0$. Since the exact distribution of T_l values is not known in the region where T_l changes rapidly from 1 to 0, the sharp cutoff approximation is made which results in the expression

$$\sigma_{\text{fus}} \simeq \pi \lambdabar^2 (J_c + 1)^2\,. \qquad (2)$$

In evaluating Eq. (2), J_c is allowed to take on nonintegral values. The J_c values extracted using Eq. (2) are presented in column 5 of Table I; the errors are derived from the corresponding uncertainties on σ_{fus}.

The total reaction cross section is the sum of the fusion and direct-reaction components and may be compared with the total reaction cross section predicted by the optical model. A precision measurement of the elastic scattering was therefore made at an energy of $E_{^{14}\text{N}} = 145.5$ MeV and is shown in Fig. 7.

IV. KINEMATICS OF THE EVAPORATION RESIDUES

The kinematical considerations for the identification of the evaporation-residue components can be discussed in a more quantitative basis by the use of the velocity diagram shown in Fig. 8. V_C and V_R are the velocities in the laboratory system of the compound nucleus and evaporation residue, respectively, while θ_L is the laboratory angle of the residue and $\theta_{\text{c.m.}}$ is the center-of-mass angle of the resultant recoil velocity v_r given to the residue by the emission of several light particles. The value of the recoil velocity v_r and angle $\theta_{\text{c.m.}}$ depend on a complicated mechanism of multiparticle evaporation. There is, therefore, no simple analytical expression for them. However, there are simple kinematical considerations which govern the extreme limits for these velocities.

The magnitude of the recoil velocity v_r is limited by a maximum value v_{max} given by the requirement

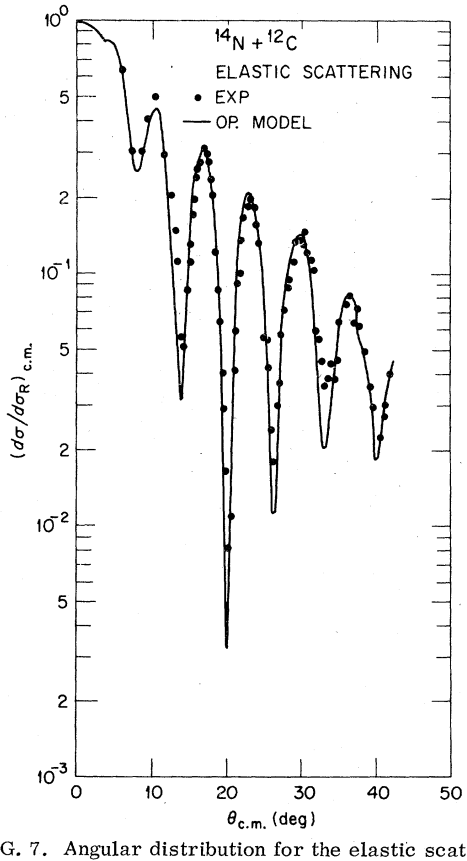

FIG. 7. Angular distribution for the elastic scattering of ^{14}N + ^{12}C at $E_{^{14}\text{N}} = 145.5$ MeV. The solid line corresponds to an optical-model fit using the parameters $V = 22.04$, $r_0 = 1.25$, $a_0 = 0.52$, $W = 14.72$, $r_i = 1.22$, and $a_i = 0.54$, in units of MeV and fm. The deduced total reaction cross section is 1398 mb.

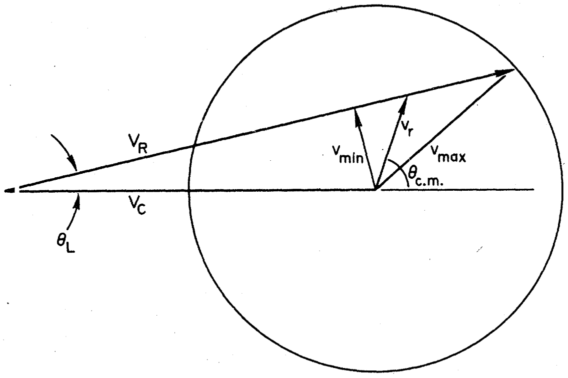

IG. 8. Velocity diagram used to discuss the simple kinematical properties of evaporation residues. V_C and V_R are the laboratory velocities of the compound nucleus and residue, respectively.

that a residue be produced in its ground state and that all recoil velocities are collinear. If $\epsilon_{\max}$ is the maximum kinetic energy released by the evaporated particles to produce a given residue of mass M_R in its ground state, then

$$\epsilon_{\max} = E_x - (M_e + M_R - M_C)c^2 , \tag{3}$$

where E_x is the excitation energy of the compound nucleus and M_R, M_C, and M_e are the masses of the evaporation residue, the compound nucleus, and the sum of all light particles evaporated, respectively. Assuming all recoil velocities are collinear, and using two-body kinematics, the maximum recoil $v_{\max}$ is given by

$$v_{\max} = (2M_e \epsilon_{\max}/M_R M_C)^{1/2} . \tag{4}$$

Furthermore, using the velocity diagram of Fig. 8 we obtain

$$V_R = V_C \cos\theta_L \pm (v_r^2 - V_C^2 \sin^2\theta_L)^{1/2} . \tag{5}$$

The maximum laboratory angle $\theta_{\max}$ for the residue is thus given by

$$\sin\theta_{\max} = v_{\max}/V_C \tag{6}$$

for $v_{\max} \leq V_C$.

The kinematic quantities of interest for the evaporation residues are the centroids and widths of the energy distributions as well as the slope of the angular distribution. Although these quantities are predicted in detail by the Monte Carlo calculations to be described in the next section, simple arguments can be used to derive analytical expressions that account for some of the main kinematic features.

Ideally, one would like to have an analytical expression for the distribution of the recoil velocity $\vec{v}_r$ that would incorporate the effects of sequential evaporation. Lacking this, a first step is to assume that the angular distributions for all emitted light particles are isotropic in the center of mass. In this case, the central-limit theorem yields a Gaussian distribution for the volume probability for $\vec{v}_r$; this probability distribution can be written as

$$\frac{d^2\sigma}{d\Omega_{\text{c.m.}} dv_r} = K v_r^2 e \left(-\frac{v_r^2}{2s^2}\right) , \tag{7}$$

where K is a normalization constant, and the standard deviation of the recoil velocity distribution s depends on the details of the evaporation mechanism and, in the present work, can be regarded as an empirical parameter.

Transformation of Eq. (7) to the laboratory system, together with Eq. (5), yields the distributions of laboratory recoil velocities V_R

$$\frac{d^2\sigma}{d\Omega_L dV_R} = K V_R^2 \exp[-V_C^2 \sin^2\theta_L/2s^2] \times \exp[-(V_R - V_C \cos\theta_L)/2s^2] \tag{8}$$

Note that the velocity dependence of the quantity $V_R^{-2} d^2\sigma/d\Omega_L dV_R$ will be given by the Gaussian term on the right-hand side of Eq. (8). Using the values for the mass number A given in Table II, the experimental energy distributions were transformed to a $V_R^{-2} d^2\sigma/d\Omega_L dV_R$ plot and then fitted

TABLE II. Kinematic properties of evaporation residues for the ^{14}N+^{12}C system.

E_{lab} (MeV)	θ_L	Z	A	E_0 (MeV)	$\bar{E}_r$ (MeV) (Exp)	$\theta_{\max}$ (Calc)	$\theta_{\max}$ (Exp)
53.2	5°	12	24	26.2	26	16	18
53.2	5°	11	23	24.9	24	26 [a]	27
86.3	9°	10	21	36.3	39	26.5	30
86.3	9°	9	18	31.2	33	37	36
145.5	10°	9	18	53	57	37	36
145.5	10°	8	16	46.7	48	41.2	43
145.5	10°	7	14	40.9	42	54	b
145.5	10°	6	12	35.0 (48)	45	57.1	b

[a] Calculated for ^{22}Na.

[b] Maximum angle measured 45°.

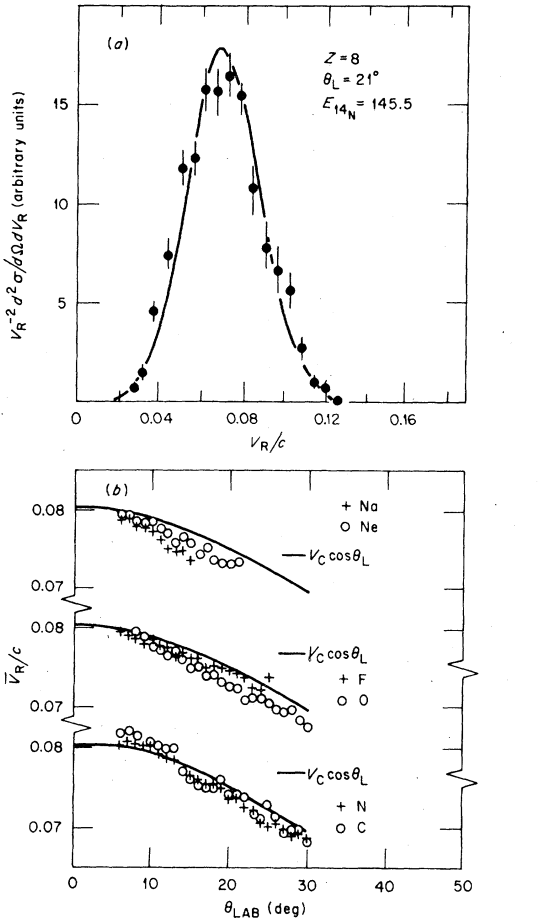

FIG. 9. (a) Plot of the velocity distribution $V_R^{-2}d^2\sigma/d\Omega dV_R$ for oxygen ions at $\theta_{\rm lab}$ = 21° and $E_{^{14}\rm N}$ at 145.5 MeV. The solid line is the result of a Gaussian fit to the data to extract the centroid $\bar{V}_R$. (b) Extracted centroids $\bar{V}_R$ for evaporation residues for Z = 6 to 11 for $E_{^{14}\rm N}$ = 145.5 MeV. The solid lines are the predicted centroids $\bar{V}_R = V_C \cos\theta_{\rm lab}$, in units of the velocity of light.

with a Gaussian term. An example of this is shown in Fig. 9(a). The resulting centroids ($\bar{V}_R$) are given in Fig. 9(b) (data points) as a function of laboratory angles for the data taken at 145.5 MeV and for all residues from $Z = 11$ to $Z = 6$. The solid curve corresponds to $\bar{V}_R = V_C \cos\theta_L$, the expected centroid from Eq. (8). The fact that the experimental points lie along such a curve indicates that the evaporation residues have the same velocity as the compound nucleus (V_C), with the cos θ_L term arising from kinematic effects. The result that V_C cos θ_L gives the average velocity of the evaporation residues can be also illustrated by the double kinematic solution of Eq. (5), since the ± solutions correspond to backward and forward emission of the light particles, respectively. Assuming that the emission process is symmetric about $\theta_{\rm c.m.} = 90°$, the two solutions are equally probable and hence $\bar{V}_R = V_C \cos\theta_L$.

Equation (8) can be expressed in terms of the kinetic energies E_R and E_C of the residues and compound nuclei, respectively. Equation (8) then becomes

$$\frac{d^2\sigma}{d\Omega_L dE_R} = \frac{K(2E_R)^{1/2}}{M_R^{3/2}} \exp[-E_C \sin^2\theta_L/s^2M_C] \times \exp[-(E_R^{1/2}-E_0^{1/2})^2/s^2M_R]\,, \qquad (9)$$

where E_0 is given by

$$E_0 = \frac{M_R E_C}{M_C} \cos^2\theta_L\,. \qquad (10)$$

For cases where the range of energies E_R allowed by kinematics [as deduced from Eqs. (4) and (5)] is large compared to s^2M_R, then the term $E_R^{1/2}$ can be neglected. The centroid of the energy distribution will then be given simply by Eq. (10). Table II shows in column 5 the results of Eq. (10) for several examples of evaporation residues and, as can be seen, there is generally good agreement between the experimental centroids $\bar{E}_R$ (column 6) and the predicted value E_0. For the case of carbon ions at 145.5 MeV, E_0 deviates significantly from $\bar{E}_R$, and in this case Eq. (9) should be used. The value from Eq. (9) is given in parentheses. The last two columns in Table II give the results for $\theta_{\rm max}$ [Eq. (6)] and for the experimental maximum angles.

Equation (9) can be used to fit the experimental energy distributions with two free parameters, K and s. However, the predicted angular distributions, obtained by integrating Eq. (9) over E_R, do not agree with the experimental ones. The difficulty with Eq. (9) in this regard is the assumption of isotropic emission implicit in Eq. (7). In fact, compound nuclei formed with large angular momentum will not have an isotropic emission of light particles. If one allows for a small anisotropy in the final c.m. angular distributions, the prediction of the angular distribution of the evaporation residues is improved. A further discussion of analytical approaches to the evaporation process, as well as a physical interpretation of s [such as that given in Ref. 15 where a similar expression to Eq. (9) is used], is beyond the scope of the present work and will be given in a future publication.

V. ANALYSIS OF THE EVAPORATION RESIDUES

A. Hauser-Feshbach Monte Carlo calculation

Even though the fusion and direct-reaction components for products with $Z \geqslant 5$ could be identified using the kinematical considerations described previously, it is of value to compare statistical-model calculations with the experimental results for the fusion component. Such a procedure enables one to determine whether the shape of the deduced energy distributions and angular distributions are consistent with those expected for evaporation residues. For these purposes a computer code[11] LILITA has been developed to calculate the relative isotopic and elemental yields of the evaporation residues and their energy and angular distributions in the laboratory system. Results obtained with LILITA have been published previously for the evaporation residues of the $^{14}N + ^{12}C$ system.[7,12]

In the present work a general description of the calculation and a more detailed comparison to the experimental data are presented. The calculation is of the Monte Carlo type, in which the history of an excited nucleus is followed until insufficient energy remains for further particle decay. To calculate evaporation-residue cross sections, it is thus necessary to know the state (i.e., excitation energy and angular momentum) of the recoiling nucleus once a particle has been emitted and to follow the change of state of the recoiling nucleus for all subsequent particle emission. After the ith particle has been emitted, the properties of the recoiling nucleus are completely defined by a set of five quantities A_i, Z_i, E_{xi}, $\vec{J}_i$, and $\vec{V}_i$, where A_i, Z_i, and E_{xi} are the mass and charge numbers and excitation energy, respectively. $\vec{J}_i$ is the total angular momentum of the recoiling nucleus and $\vec{V}_i$ is its velocity in the laboratory system. When the next particle is emitted the nucleus changes from state "i" to "$i+1$" and the problem is to determine the new set of quantities that define the recoiling nucleus. The change in A_i and Z_i is trivial depending only on the kind of particle emitted (α'). In the present calculation the emission of neutrons, protons, or α particles has been included. The change in the excitation energy E_{xi}, the angular momentum $\vec{J}_i$, and the recoil velocity $\vec{V}_{\alpha'}$ can be determined from the amounts of orbital angular momentum $\vec{l}_{\alpha'}$ and kinetic energy $\epsilon_{\alpha'}$ (measured in the c.m. of the recoiling nucleus) carried away by the light particle. Clearly the change from state i to $i+1$ depends on the probability $P(\alpha, \vec{l}_{\alpha'}, \epsilon_{\alpha'}, \vec{V}_{\alpha'})$ for a given $\vec{J}_i$ and E_{xi}. Rather than calculate P for all possible combinations of its variables as well as for all possible numbers of emitted particles, the present approach consists of using the Monte Carlo method in conjunction with probability distributions derived from the Hauser-Feshbach formula.

The starting point in the calculation consists in the determination of the initial state, $i=0$ (the compound nucleus). The quantities A_0, Z_0, E_{x0}, and $\vec{V}_0$ are completely fixed by the entrance channel. The distribution of the total angular momentum J_0 is governed by Eq. (1). Using the sharp cutoff model for Eq. (1), together with Eq. (2), the probability distribution P_{J_0} can be written

$$P_{J_0} = (2J_0+1)/(J_c+1)^2 \,. \tag{11}$$

The probability distribution for α' and $l_{\alpha'}$ at any step i of the evaporation process can be written as

$$P_{J_i}(\alpha', l_{\alpha'}) = F_{J_i}(\alpha', l_{\alpha'}) \Big/ \sum_{\alpha'', l_{\alpha''}} F_{J_i}(\alpha'', l_{\alpha''}) \,, \tag{12}$$

where the function F is defined by

$$F_{J_i}(\alpha', l_{\alpha'}) = \int d\epsilon_{\alpha'} \sum_{S_{\alpha'}, J_{i+1}} \rho(\epsilon_{\alpha'}, J_{i+1}) T_{l_{\alpha'}} \tag{13}$$

and $\vec{J}_i = \vec{l}_{\alpha'} + \vec{S}_{\alpha'}$. The channel spin $S_{\alpha'}$ is given by J_{i+1} or $J_{i+1} \pm \frac{1}{2}$ for α-particle emission or proton and neutron emission, respectively. The quantities ρ and $T_{l_{\alpha'}}$ are the level density in the $i+1$ nucleus and the optical-model transmission coefficient. With J_i known, α' and $l_{\alpha'}$ having been chosen according to Eq. (12), $\epsilon_{\alpha'}$ and J_{i+1} can then be determined from their respective probability distributions $P_{\epsilon_{\alpha'}}$ and $P_{J_{i+1}}$. These are given by

$$P_{\epsilon_{\alpha'}} = \sum_{S_{\alpha'}, J_{i+1}} \rho(\epsilon_{\alpha'}, J_{i+1}) T_{l_{\alpha'}}(\epsilon_{\alpha'}) \Big/ F_{J_i}(\alpha', l_{\alpha'}) \tag{14}$$

and

$$P_{J_{i+1}} = \rho(\epsilon_{\alpha'}, J_{i+1}) \Big/ \sum_{J_{i+1}} \rho(\epsilon_{\alpha'}, J_{i+1}) \,. \tag{15}$$

Equations (12) to (15) are applied sequentially until the excitation energy of the recoiling nucleus is at or below the point where particle decay is no longer possible.

The usual procedure for evaluating the level density ρ and the transmission coefficients $T_{l_{\alpha'}}$ is to use the Fermi-gas formula (see Ref. 16), and to solve the Schrödinger equation for the optical-model transmission coefficients, respectively. However, this procedure would lead to unreasonably long computing times for cases where the excitation energy and angular momentum of the compound nucleus are high, since many particles are emitted before a residue is produced. It is for this reason that the present calculations were done using a constant temperature approximation for ρ (see Refs. 17 and 18) and the sharp cutoff model for $T_{l_{\alpha'}}$ for excitation energies in the continuum region. For excitation energies below the continuum (i.e., the region of discrete levels), an energy-independent density for ρ and a Fermi function for $T_{l_{\alpha'}}$ were used. With these approximations, Eq. (13) can be integrated analytically over $\epsilon_{\alpha'}$, thus leading to a significant reduction in computing time. The parameters describing the level densities were taken from well-known systematics[18,19] for the continuum region and $A > 20$, and were obtained by fits to known experimental levels for discrete regions and $A < 20$ using the compilations of Endt and Van der Leun[20] and Ajzenberg-Selove.[21] The possibility of γ decay by levels above the threshold for particle emission was included explicitly, with values of $\Gamma_\gamma/\Gamma_{\text{tot}}$ taken from Refs. 20 and 21. This turned out to be of minor consequence for the light nuclei encountered in this study. The radial parameter $r_0 = 1.5$ was used for the calculation of Coulomb and centrifugal barriers, while $r_0 = 1.4$ fm was used for the rigid body nuclear moment of inertia.

The recoil velocity $\vec{V}_i$ is calculated from the velocity of the light particle $\vec{v}_{\alpha'}$ (defined in the c.m. system of the recoiling nucleus). The magnitude of $v_{\alpha'}$ was obtained from $\epsilon_{\alpha'}$. The remaining unknowns are the polar angle ν and azimuthal angle δ. These angles are calculated using the classical approach of Ericson and Strutinski.[22] Choosing the polar axis in the direction of the total angular momentum $\vec{J}_i$, the azimuthal angle δ at which a particle is emitted has an isotropic probability distribution since the system has to be rotationally invariant with respect to J_i. The probability distribution for ν is determined using the angular distribution given in Ref. 22 and can be written

$$\frac{d\sigma}{d\Omega_\nu} \propto \frac{1}{(\sin^2\nu - \cos^2\nu_l)^{1/2}}\,, \tag{16}$$

where ν_l is the polar angle between $\vec{l}_{\alpha'}$ and $\vec{J}_i$. The value of ν_l is given by the vector triangle $\vec{J}_i = \vec{l}_{\alpha'} + \vec{S}_{\alpha'}$, since the magnitudes of the three vectors are already fixed. The corresponding probability distribution P_ν can be written

$$P_\nu = \frac{2\sin\nu}{(\sin^2\nu - \cos^2\nu_l)^{1/2}}\,, \tag{17}$$

where the range of values for ν is given by $\nu_{\min} \le |\nu| \le \pi/2$ and $\cos\nu_{\min} = \sin\nu_l$. The recoil velocity in the c.m. system $\vec{v}_{r'}$ is determined from $\vec{V}_{\alpha'}$ by a simple reflection of coordinates. To calculate $\vec{V}_i$ it is necessary to transform $\vec{v}_{r'}$ to a vector $\vec{v}_r$ defined in the laboratory axes. Denoting the matrix of such a transformation as A_i^{-1}, we have $\vec{V}_i = \vec{V}_{i-1} + \vec{v}_r$,

$$\vec{v}_r = A_i^{-1}\vec{v}_{r'}\,, \tag{18}$$

and

$$A_i = \prod_{n=0}^{i-1} R_n\,, \tag{19}$$

where R_n are rotational matrices of the angles ν_j and δ. Here, ν_j is the polar angle between $\vec{J}_i$ and $\vec{J}_{i+1}$. As is the case with ν_l, ν_j is determined by a vector triangle and the magnitudes of J_i, $l_{\alpha'}$, and $S_{\alpha'}$. The initial condition ($i = 0$) has the polar axis perpendicular to the reaction plane, the Y axis along the beam direction, $\delta = 0$, and $R_0 = 1$. The solutions of Eqs. (12) through (19) for a sequence of evaporated particles produces a residue (event) in a final state f characterized by A_f, Z_f, Ex_f, $\vec{J}_f$, and $\vec{V}_f$. The procedure is then repeated until a sufficient number of events has been generated in order to make a statistically significant comparison to the data. For the present calculations 10^4 events were generated for comparisons to relative yields and 10^5 events for energy and angular distributions.

B. Discussion of the fusion data and comparison with Hauser-Feshbach calculations

A comparison between the Hauser-Feshbach calculations and the experimental data for the relative yields of the evaporation residues is shown in Fig. 10 for residues from $Z = 5-12$ and

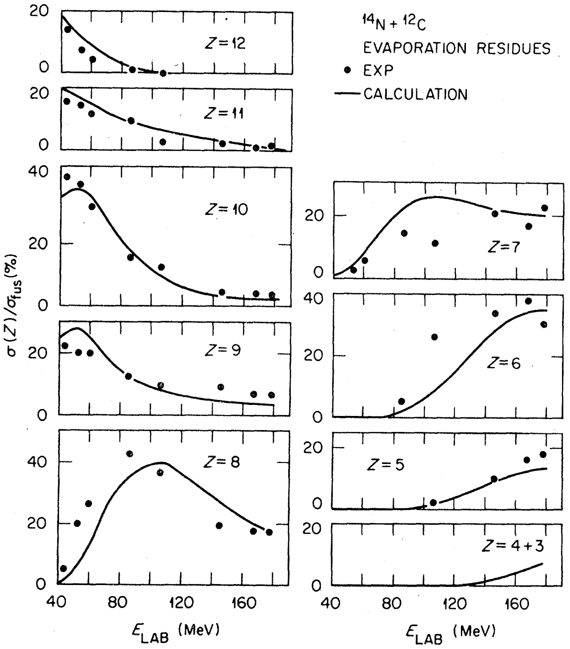

FIG. 10. Angle-integrated yields for evaporation residues with $Z = 5$ to 12, expressed as a percentage of σ_{fus} for $E_{^{14}\text{N}}$ energies from 40 to 180 MeV. The solid lines are the results of the Monte Carlo Hauser-Feshbach calculations described in the text.

for $E_{^{14}N}$ bombarding energies from 40 to 180 MeV. The yields for $Z = 13$ are not included since they represent less than 1% of σ_{fus} at all energies in the experimental and calculated yields. The agreement between the calculations (solid lines) and experiment is better than 30% for most ions from $Z = 5$ to $Z = 12$ for the entire bombarding energy range. The largest discrepancies (about a factor of 2) occur for $Z = 6$, 7, and 8 in the bombarding energy range from 40 to 120 MeV. However, it should be noted that the theoretical predictions are lower for $Z = 8$ and $Z = 6$ by about the same amount as the excess predicted for $Z = 7$. Since the trend in bombarding energy for the data shown in Fig. 10 is well reproduced by the calculations, we expect that the discrepancies just mentioned come from uncertainties in the parameters used to describe the discrete region, rather than arising from the presence of nonfusion components.

To further illustrate the agreement between the Hauser-Feshbach calculations and the evaporation-residue data, Fig. 11 shows the Z distributions for two extreme bombarding energies, 43.9 and 178.1 MeV. As can be seen, the maxima and dispersion of the Z distribution are well reproduced by the calculations indicating that these residues are consistent with an equilibrated compound nucleus. The comparisons for the energy and angular distributions are shown in Figs. 3 and 4 for the data at 53.2 and 145.5 MeV, respectively. The residues for $Z = 10-12$ for the bombarding energy of 53.2 MeV obviously have energy spectra characteristic of evaporation residues and, as can be seen from Fig. 3, the Monte Carlo calculations (histograms) reproduce the experimental data reasonably well. (The calculated cross sections at 5° for $Z = 11$ and $Z = 12$ have been arbitrarily normalized to the data by factors of 0.5 and 1.5, respectively, only to enable a better shape comparison to the energy distributions.) The angle-integrated yields shown in Fig. 10 are expressed as a percentage of the total fusion cross section, where both the experimental and theoretical total fusion cross sections are normalized to 100%.

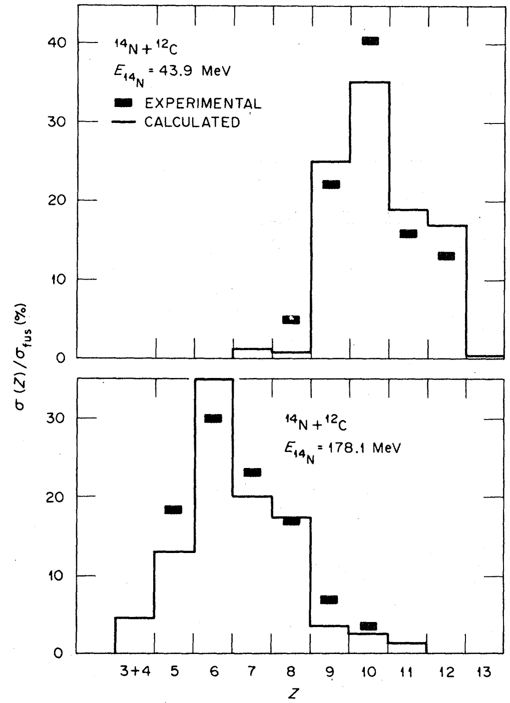

FIG. 11. Angle-integrated yields for evaporation residues with $Z = 5$ to 12 expressed as a percentage of σ_{fus}, for two extreme bombarding energies of 43.9 and 178.1 MeV. The histograms are the results of the Monte Carlo Hauser-Feshbach calculations described in the text.

A comparison between the experimental angular distributions and the calculations for $E_{^{14}N} = 53.2$ MeV is given on the left-hand side of Fig. 3. The agreement is particularly striking for the Ne yield. At this energy the Ne cross section accounts for almost 40% of σ_{fus}. The double structure seen in the angular distribution for Na ions (and reproduced by the calculations) comes from the $2p$, $2pn$, and from α, αn channels with the most forward peaked component corresponding to $2p$, $2pn$ emission. The calculated angular distribution for Mg ions has been multiplied by 0.5 because at this energy the calculation predicts more pn emission than $2p$; however, these predictions could be improved by small adjustment of the relevant level density parameters. Since the general procedure adopted in the calculation was to use level density parameters from previous systematics,[18,19] no particular effort was made to optimize the fits to the experimental data.

The comparison for the energy and angular distributions at $E_{^{14}N} = 145.5$ MeV for oxygen, nitrogen, and carbon residues is shown in Fig. 4. The good agreement here is particularly important, since it shows that fusion cross sections can be extracted even for residues whose masses are comparable to or less than those of the target or projectile. As was pointed out in Ref. 7, one cannot rule out, on the basis of these single inclusive measurements, small contributions of highly inelastic two-body-like processes to the evaporation-residue spectra. However, the agreement between the calculated and experimental energy and angular distributions, as well as the agreement in the relative yields as a function of bombarding energy (Figs. 10 and 11), suggests that the major mechanisms producing the lower-energy particle groups, for isotopes of atomic number around the target or projectile, is that of evaporation of light particles by an equilibrated compound nucleus. Coincidence measurements made subsequently have confirmed the absence of significant two-body contributions with large negative Q values to the yields designated as evaporation residues.[23] "Two-body" in the foregoing refers to two large products, e.g., each with $Z \geq 5$ in the exit channel. Such products could conceivably be produced in a binary fission process followed by evaporation of a few light particles by the highly excited fission fragments.

The fusion cross sections presented in Table I are plotted as a function of $1/E_{\text{c.m.}}$ in Fig. 12(a) (open circles). The open triangles correspond to measurements at 158 and 248 MeV taken from Ref. 12, while the solid dots correspond to low-energy measurements by Kuehner and Almqvist.[24]

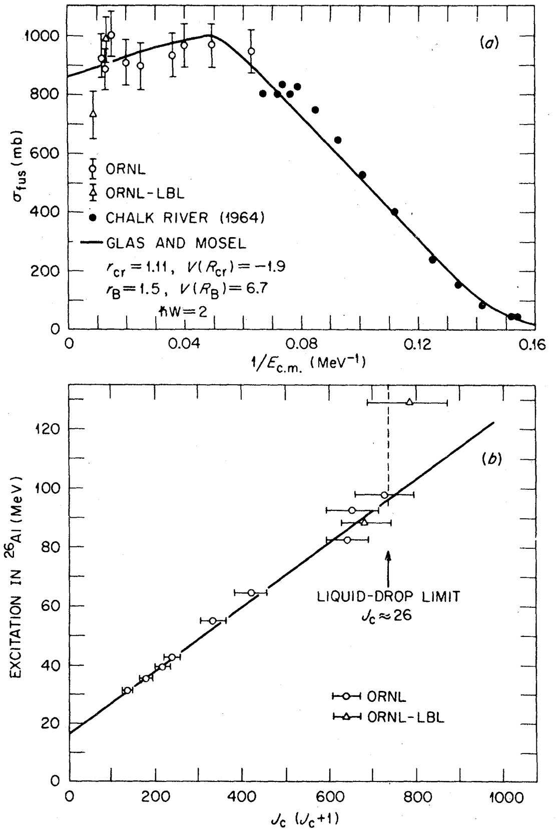

FIG. 12. (a) σ_{fus} vs $1/E_{\text{c.m.}}$. The open circles correspond to the present measurements, the triangles to those of Ref. 12, and the solid points to those of Ref. 24. (b) Values of the critical angular momentum J_c [plotted as J_c (J_c+1)] vs the excitation energy in ^{26}Al. The solid line is a fit to all data points except the point at 130 MeV excitation.

One possible way to parametrize the energy dependence of the fusion cross section is to assume that fusion occurs when the relative separation of the two nuclei reaches a critical radius R_{cr}.[25,26] Using the model of Glas and Mosel[26] it is possible to relate the magnitude of the Coulomb-plus-nuclear potential V_{cr} at R_{cr} to the magnitude and slope of σ_{fus} (E) for energies larger than the interaction barrier. Following Ref. 26, the fusion cross section as a function of the center-of-mass energy can be written as

$$\sigma_{\text{fus}} = \pi \lambda\!\!\!^{-2} \sum_{l=0}^{l_c} (2l+1) \Big/ \{1 + \exp[2(V_{Bl} - E_{\text{c.m.}})/\hbar\omega]\} \tag{20}$$

where l_c, the critical angular momentum, is given by

$$l_c(l_c+1) = (2\mu R_{\text{cr}}^2/\hbar^2)(E_{\text{c.m.}} - V_{\text{cr}}) \tag{21}$$

and V_{Bl} is given by

$$V_{Bl} = V_B + \hbar^2 l(l+1)/2\mu R_B^{\,2}, \tag{22}$$

where V_B is the interaction barrier and $R_{\text{cr}} = r_{\text{cr}}(A_1^{1/3} + A_2^{1/2})$, $R_B = r_B(A_1^{1/3} + A_2^{1/3})$, and μ is the reduced mass in the entrance channel.

The solid curve drawn through the data points in Fig. 12(a) is the result of a fit of Eq. (20) to the experimental fusion cross section with the parameters $V_{\text{cr}} = -1.9$ MeV, $r_{\text{cr}} = 1.11$, $r_B = 1.5$, $V_B = 6.7$, and $\hbar\omega = 2$ MeV. Although the experimental fusion cross section is consistent with the Glas-Mosel prediction up to $E_{^{14}\text{N}} = 178.1$ $(1/E_{\text{c.m.}} = 0.012)$, the critical radius r_{cr} is slightly higher than the value of 1.0 deduced for heavier systems.[26]

In Ref. 7 it was noted that the deduced value of the nuclear potential at the critical radius was consistent with a shallow Woods-Saxon potential of the type introduced by Maher *et al.*,[27] whereas elastic scattering measurements for the system ^{12}C + ^{12}C indicate a much deeper potential.[28] At least a part of this discrepancy may arise from the neglect of nonconservative interactions (i.e., friction) in the Glas-Mosel prescription. The introduction of friction would require a more negative value of the nuclear potential in order to fit the experimental data (see Ref. 29).

As noted in Ref. 12, the fusion cross section at $E_{^{14}\text{N}} = 248$ MeV (717 ± 85 mb) shows a marked decrease from the value predicted by the Glas-Mosel fit to the lower energies, thus indicating that a limit lower than that imposed by the entrance channel is occurring.

The values of J_c deduced from σ_{fus} and given in Table I are shown in Fig. 12(b) as a function of the excitation energy in ^{26}Al. The open circles correspond to the present measurements and the triangles to those in Ref. 12. The solid line drawn through the data points is a least-squares fit of the function $E_x = (\hbar^2/2\mathcal{I})\,J(J+1)+E_0$, where the values of E_0 and $2\mathcal{I}/\hbar^2$ are 16 MeV and 9.19 MeV^{-1}, respectively. Since the $J_c(J_c+1)$ vs E_x line suggests rigid rotation, an alternative explanation to the limitation of σ_{fus} would appear to be the maximum angular momentum that the compound nucleus ^{26}Al can have at a given excitation energy (i.e., the location of the yrast line). The value of the moment of inertia $\mathcal{I}/\hbar^2$ deduced from the measurements of σ_{fus} is approximately twice as large as that deduced for the ground state band (calculated by fitting the known 5^+, 6^+, and 7^+ states[20]). The yrast line, of course, must be at or below the line shown in Fig. 12(b). Recent calculations by Glas and Mosel[30] suggest that the yrast line is well below the fusion values; this implies that the limitation occurs with the entrance channel rather than the compound nucleus, at least for energies up to 178 MeV.

For the highest excitation energy (~130 MeV) a sudden change is observed in the slope of $J_c(J_c+1)$ vs E_x, and J_c appears to remain constant for $E_x > 100$ MeV at a value of $J_c \simeq 27\,\hbar$. As discussed in Ref. 12, this fact (associated with the drop on σ_{fus} at $E_{^{14}\mathrm{N}} = 248$ MeV) suggests the maximum angular momentum which ^{26}Al can support has been observed.

It is commonly accepted that a nucleus spinning with increasing angular momentum J will at some point, $J_{\max}$, become unstable to fission into two comparable fragments. Conversely, we expect that such a nucleus would not be formed (in equilibrium) in a heavy-ion reaction proceeding by the fusion of these two fragments. Currently, the model which is used to estimate $J_{\max}$ is the rotating liquid-drop model (RLDM).[13] The suitability of such a model for systems with a small nucleon number can be questioned. While the RLDM may be appropriate for a spherical ^{26}Al nucleus, the number of nucleons contained in the neck region at the saddle point configuration at $J = J_{\max}$ is between 10 and 15% of the total number of nucleons. Nevertheless, it is interesting to note that the value of $J_{\max}$ predicted by RLDM, $26.6\hbar$, agrees with the experimental value of $(27 \pm 1.5)\hbar$.

Predictions of the fusion cross sections for ^{14}N + ^{12}C have been made in the time dependent Hartree-Fock (TDHF) approximation.[31] These calculations overestimate σ_{fus} by amounts up to 30%. A gradual decrease in σ_{fus} with increasing bombarding energy is predicted, in contrast with the rapid drop observed experimentally between $E_{^{14}\mathrm{N}} = 178$ and 248 MeV.

VI. DIRECT-REACTION DATA AND ANALYSIS

The direct-reaction components, which have a centroid characteristic of the velocity of the projectile, are illustrated in the energy distributions of Fig. 4 and in the angular distributions of Fig. 6. A further example at a more forward angle, 5°, is shown in Fig. 13 for the energy distributions of $Z = 5$ to $Z = 8$ at a bombarding energy of 145.5 MeV. The dashed lines in the figure indicate the unfolding of the evaporation residues and direct components. The sharp peaks in the energy spectrum of $Z = 6$ to $Z = 8$ arise from transfer reactions to specific states or clusters of states in the residual nuclei. An interesting feature of the energy distributions of Fig. 13 is the presence of a continuous distribution underlying the discrete peaks at high ejectile energies (particularly prominent for $Z = 6$).

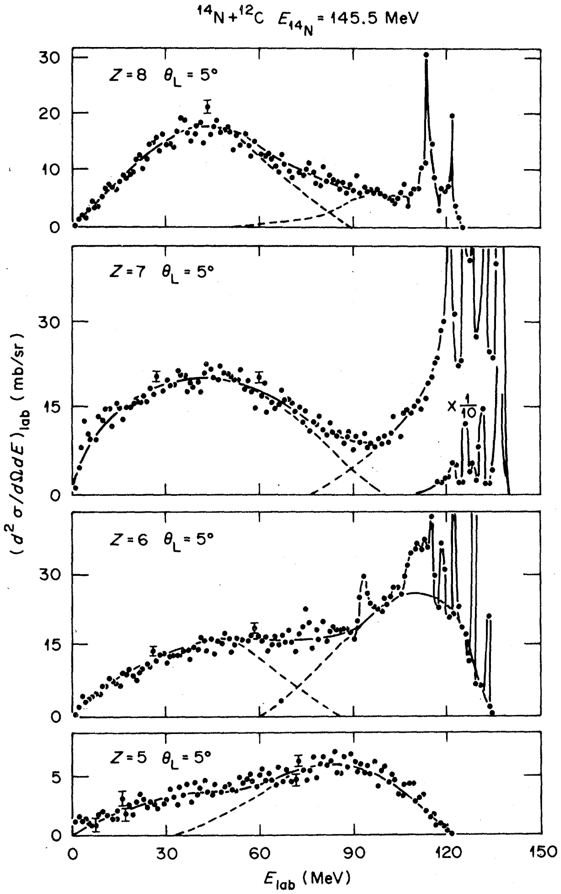

FIG. 13. Energy distributions for $Z = 5$ to 8 at $E_{^{14}\mathrm{N}} = 145.5$ and $\theta_{lab} = 5°$. The dashed line at lower energies corresponds to the unfolding of the evaporation residues. The remainder of the yield at higher energies represents the direct component. The dashed lines at higher energies illustrates the direct continuum underlying the selective population of discrete states.

We expect that the discrete particle groups seen in the $Z = 6$ spectrum of Fig. 13 arise from the transfer of a proton (and an undertermined number of neutrons) to form selectively excited states in C or N isotopes. The underlying continuum, however, may contain contributions not only from the dense continuum states in these isotopes, but also from the excitation of the ^{14}N projectile and subsequent nucleon decay of this fragment.

The angular distributions such as those seen in Fig. 6 were obtained by summing the continuous and discrete portions of the high-energy component. The contribution of the low-energy recoiling partner to the direct-reaction yield is negligible.

A simple diffraction-model analysis[32] was carried out for the data shown in Fig. 6. In this approach the slope of the angular distribution is given for the inelastic channels by the damping factors

$$\frac{d\sigma}{d\Omega} \propto \frac{\theta_{\mathrm{c.m.}}}{\sinh^2(\pi\Delta\theta_{\mathrm{c.m.}})} \tag{23}$$

and by

$$\frac{d\sigma}{d\Omega} \propto \frac{1}{\theta_{\mathrm{c.m.}}\sinh^2(\pi\Delta\theta_{\mathrm{c.m.}})} \tag{24}$$

for elastic scattering. The center-of-mass scattering angle is $\theta_{\mathrm{c.m.}}$ and Δ is related to the modulus of the scattering matrix by[32]

$$|S_l| = \frac{1}{1+\exp[(L-l)/\Delta]}\ . \tag{25}$$

The oscillations of the cross sections about the damping factor expected for population of a single state and described by a Bessel function are neglected in the analysis. In order to obtain Δ, the S_l were determined by fitting the elastic scattering at 145.5 MeV with the optical model, as shown in Fig. 7. The deduced optical-model parameters from the elastic scattering were $V = 22.04$ MeV, $r_0 = 1.25$, and $a_0 = 0.52$ for the real part and $W = 14.72$, $r_i = 1.22$, and $a_i = 0.54$ for the imaginary part. With these parameters, the deduced value of Δ was 1.4.

The result of the diffraction-model calculations for the elastic scattering [Eq. (24)] is shown in Fig. 14 and for the inelastic channels [Eq. (23)] in Fig. 6. For $Z = 5$, the slope of the data for the angular distribution is much smaller than that given by Eq. (23). This may be interpreted as a result of particle emission from the excited fragment produced in the direct collision. The general agreement between the diffraction calculation and the data of Figs. 6 and 14 indicates that the basic mechanism producing the higher-energy components of Figs. 4 and 13 is that of a direct reaction.

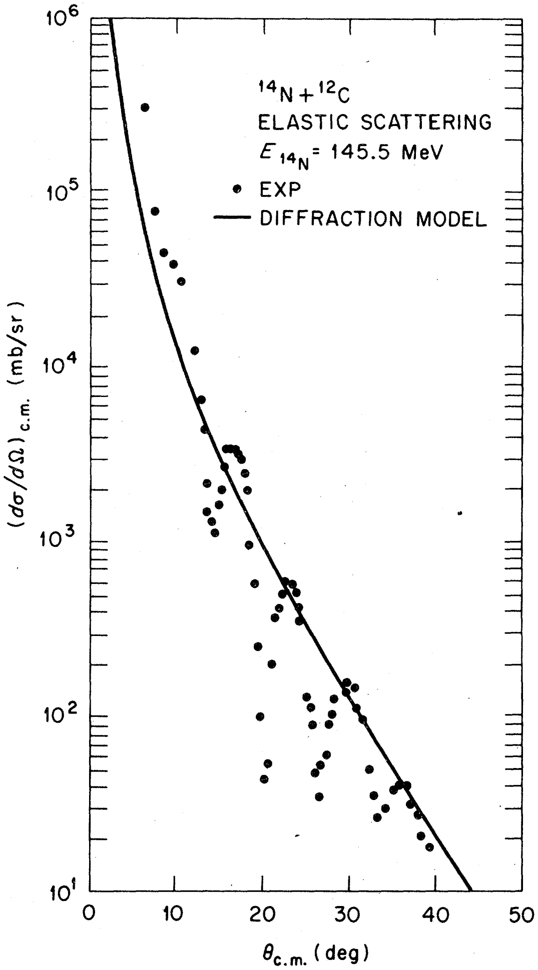

FIG. 14. The elastic scattering at $E_{^{14}\mathrm{N}} = 145.5$. The solid line is the damping factor from the diffraction model.

Table III shows the contribution (in mb) to the total direct component for ions from $Z = 5$ to $Z = 8$ at four bombarding energies, 106.3, 145.5, 167.3, and 178.1 MeV.

Time-dependent Hartree-Fock (TDHF) calculations have been made for our fusion data and also for the direct inelastic yield for $Z = 7$ by Maruhn-

TABLE III. Direct-reaction cross sections σ_D for the ^{14}N + ^{12}C system.

		E_{lab} (MeV)			
		106.3	145.5	167.3	178.1
Z	8	6	25	17	23
	7	209	119	150	162
	6	178	155	112	145
	5	47	49	49	58
σ_D		440 ± 40	348 ± 28	328 ± 26	338 ± 31

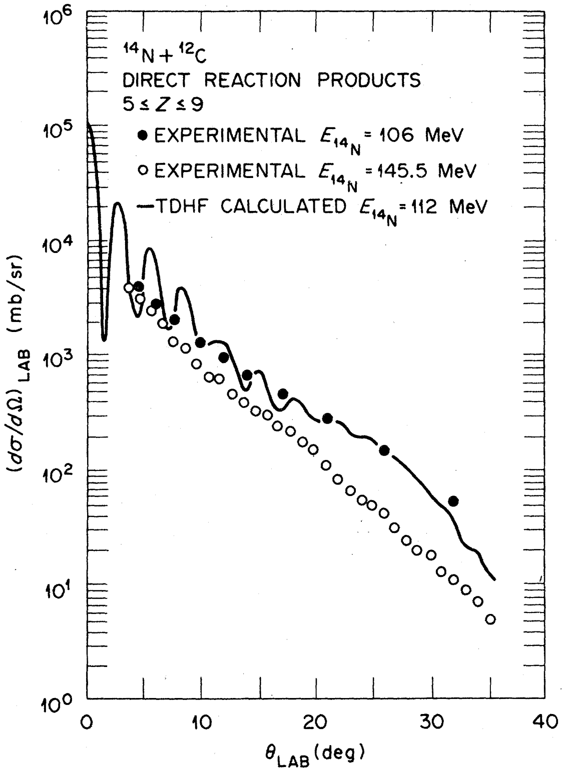

FIG. 15. Comparison of the direct-reaction angular distribution, summed over all isotopes from Z = 5 to 9, with TDHF calculations (Ref. 33).

Rezwani *et al.*[31] The calculated direct inelastic angular distribution had a $1/\sin\theta$ shape, in disagreement with experiment. Recently, Cusson[33] has improved the TDHF calculations allowing for quantal corrections. Figure 15 shows the comparison between our direct-reaction data at 106 and 145.5 MeV and the TDHF calculations[33] for E_{14_N} = 112 MeV. The TDHF calculations correspond to a direct inelastic excitation of the projectile and target to all available excited states. These calculations do not predict mass transfer nor do they incorporate any subsequent particle decay of the excited ^{14}N and ^{12}C fragments. In order to establish a meaningful comparison with theory we have therefore summed over all direct-reaction channels. As can be seen from Fig. 15, the slope of the TDHF calculation is in reasonable agreement with the data at 106 MeV. Up to this energy the direct-reaction components have been extracted only for isotopes $Z \geq 5$. The sum of these contributions is labeled σ_D and is given in column 3 of Table IV.

VII. THE TOTAL REACTION CROSS SECTION

TABLE IV. Summary of cross section measurements for the $^{14}N+^{12}C$ system.

E_{lab}	σ_{fus}	σ_D	$\sigma^D_{\text{Li,Be}}$	σ_r	σ_r [a] (O.M.)
34.1	945	$\cdots$	$\cdots$	945	950
43.9	967	140	$\cdots$	1107	1080
53.2	964	300	$\cdots$	1264	1170
60.0	932	320	$\cdots$	1252	1218
86.3	895	400	19	1314	1322
106.3	913	440	37	1390	1373
145.5	1005	348	88	1441	1450
167.1	888	328	95	1311	1468
178.1	932	388	88	1408	1482

[a] Optical-model parameters from Ref. 28.

In this section we deduce the total reaction cross section and begin with a discussion of the origin of the Li and Be yields. As was pointed out in Ref. 4, the yields of $^{6,7}Li$ and $^{7,9}Be$ cannot be accounted for completely by a process of first or second chance emission from the compound nucleus. The integrated yields of Li and Be from the present experiment are plotted in Fig. 16 for the E_{14_N} range of 86 to 178 MeV, and the open circles correspond to Hauser-Feshbach calculations (given in Ref. 4) for emission of Li and Be from the compound nucleus and, as can be seen, the calculations are about three times smaller than the experimental values for the highest en-

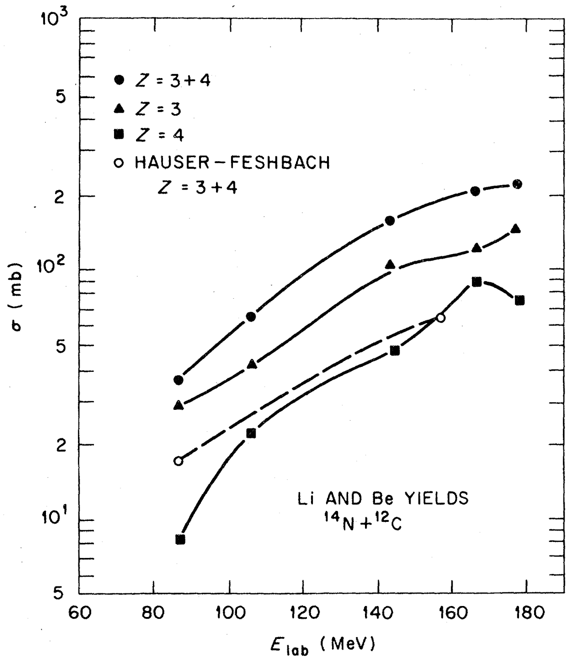

FIG. 16. The yields in mb of Li and Be as a function of the bombarding energy. The squares and triangles correspond to the Be and Li yields, respectively. The solid circles are the experimental sum of Li and Be and are to be compared with the open circles corresponding to Hauser-Feshbach calculations given in Ref. 4.

ergy. Also, the additional yield expected for evaporation residues of $Z=3$ or 4 is too small (see Fig. 10) to account for the experimental yield. These facts suggest that the excess yield must come from a fragmentation of those direct-reaction products which have sufficient excitation for particle emission.

Column 4 of Table IV shows as $\sigma^D_{\mathrm{Li,Be}}$ the yield of these isotopes expected to contribute to the direct-reaction cross section. This cross section is equal to the experimental value minus the yield expected from compound-nucleus evaporation. The latter may be estimated by logarithmic interpolation of the Hauser-Feshbach calculations (given in Fig. 16) and from evaporation residues (given in in Fig. 10). The sum of $\sigma_{\mathrm{fus}}+\sigma_D+\sigma^D_{\mathrm{Li,Be}}$ is the experimental total cross section σ_r and is given in column 5.

With the optical-model parameters obtained from the elastic scattering data of Fig. 7, the inferred total reaction cross section σ_r(O.M.) is 1398 mb, while using the (Woods-Saxon) optical-model parameters deduced from the $^{12}C+^{12}C$ elastic scattering[28] we obtained a value of $\sigma_r = 1440$ mb. Since at other bombarding energies we do not have elastic scattering data as complete as those given in Fig. 7, we decided to use the optical-model parameters of Ref. 28 to compute σ_r for the entire range of bombarding energy of the present experiment. Figure 17 summarizes the results of our measurements of σ_{fus}, σ_D and for the yields of Li and Be. The solid line corresponds to σ_r(O.M.). As can be seen from Fig. 17, the sum of σ_{fus} and σ_D is in agreement with the optical model up to bombarding energies of 106 MeV. However, for the higher energies the portion of the yields of Li and Be denoted by $\sigma^D_{\mathrm{Li,Be}}$ have to be included in order to account for the predicted reaction cross section. Thus, we find good agreement between the experimental total reaction cross section and the optical model.

VIII. CONCLUSION

Heavy-ion reaction products for the $^{14}N+^{12}C$ system have been measured at a total of nine bombarding energies from 34.1 to 178 MeV. The energy spectra of products with $5 \leq Z \leq 9$ often exhibit two components at forward angles which on the basis of a straightforward kinematic analysis can be identified with an evaporation residue produced in a fusion reaction and a product of a direct peripheral reaction. These same kinematic considerations verify that the products at larger angles and with $Z>9$ are evaporation residues.

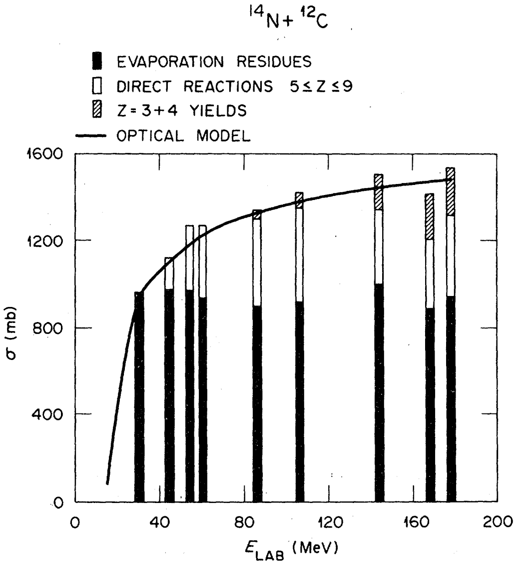

FIG. 17. Summary of cross section measurements for the $^{14}N+^{12}C$ system for $E_{^{14}N}$ energies from 34.1 to 178.1 MeV. The solid bars are σ_{fus}, the open bars correspond to σ_D, and the dashed bars to the yields of Li+ Be. The solid curve is the predicted total reaction cross section σ_r with the optical-model parameters of Ref. 28.

Thus, fusion and direct-reaction cross sections are obtained independent of detailed statistical model calculations. From a comparison of the experimental evaporation residue Z distributions and the energy and angular distributions with Monte Carlo Hauser-Feshbach calculations, it appears that, even at the highest energy, a compound nucleus is formed in statistical equilibrium. The measured fusion cross sections were found to be significantly less than the total reaction cross section. For energies up to $E_{^{14}N}=178$ MeV, the fusion cross sections appear to be limited by the entrance channel rather than by the yrast line of the compound nucleus. At energies above this, however, the experimental data indicate a limit of ~$27\hbar$, which is consistent with the predicted limiting angular momentum for a rotating liquid drop.[13] The sum of the fusion and direct components was found to be in good agreement with the total reaction cross section as given by the optical-model calculations.

Valuable discussions with W. T. Milner concerning Monte Carlo calculations are acknowledged, as well as the TDHF calculations provided by R. Y. Cusson. This research was sponsored by the U.S. Department of Energy, under Contract No. W-7405-eng-26 with the Union Carbide Corporation.

*Present address Centre d'Etudes de Bruyères-Chatel, 92542 Montrouge, France.

[1] C. Olmer, R. G. Stokstad, D. L. Hanson, K. A. Erb, M. W. Sachs, and D. A. Bromley, Phys. Rev. C 10, 1722 (1974); C. Volant, M. Conjeaud, S. Harar, S. M. Lee, A. Lepine, and E. F. de Silveira, Nucl. Phys. A238, 120 (1975); H. V. Klapdor and H. Reiss, Z. Phys. 262, 83 (1973).

[2] K. R. Cordell, S. T. Thornton, L. C. Dennis, T. C. Schweizer, J. Gomez del Campo, and J. L. C. Ford, Jr., Nucl. Phys. A296, 278 (1978).

[3] D. L. Hanson, R. G. Stokstad, K. A. Erb, C. Olmer, and D. A. Bromley, Phys. Rev. C 9, 929 (1974).

[4] R. G. Stokstad, M. N. Namboodiri, E. T. Chulick, J. B. Natowitz, and D. L. Hanson, Phys. Rev. C 16, 2249 (1977).

[5] R. G. Stokstad, in *Proceedings of the International Conference on Reactions Between Complex Nuclei, Nashville, Tennessee, 1974,* edited by R. L. Robinson, F. K. McGowan, J. B. Ball, and J. H. Hamilton (North-Holland, Amsterdam, 1974), Vol. II, p. 327.

[6] B. Tamain, C. Ngo, J. Peter, and F. Hanappe, Nucl. Phys. A252, 187 (1975), and references therein.

[7] R. G. Stokstad, J. Gomez del Campo, J. A. Biggerstaff, A. H. Snell, and P. H. Stelson, Phys. Rev. Lett. 36, 1529 (1976).

[8] A. Weidinger, F. Busch, G. Gaul, W. Trautmann, and W. Zipper, Nucl. Phys. A263, 511 (1976).

[9] M. N. Namboodiri, E. T. Chulick, and J. B. Natowitz, Nucl. Phys. A263, 491 (1976).

[10] P. Sperr, S. Vigdor, Y. Eisen, W. Henning, D. G. Kovar, T. R. Ophel, and B. Zeidman, Phys. Rev. Lett. 36, 405 (1976).

[11] J. Gomez del Campo and R. G. Stokstad (unpublished).

[12] R. G. Stokstad, R. A. Dayras, J. Gomez del Campo, P. H. Stelson, C. Olmer, and M. S. Zisman, Phys. Lett. 70B, 289 (1977); work (unpublished).

[13] S. Cohen, F. Plasil, and W. J. Swiatecki, Ann. Phys. (N.Y.) 82, 557 (1974).

[14] R. G. Stokstad, D. C. Hensley, and A. H. Snell, Nucl. Instrum. Meth. 141, 499 (1977).

[15] C. K. Gelbke, D. K. Scott, M. Bini, D. L. Hendrie, J. L. Laville, J. Mahoney, M. C. Mermaz, and C. Olmer, Phys. Lett. 70B, 475 (1977).

[16] A. Gilbert and A. G. W. Cameron, Can. J. Phys. 43, 1446 (1965).

[17] K. A. Eberhard, P. von Bretano, M. Bohning, and R. O. Stephen, Nucl. Phys. A125, 673 (1969).

[18] J. R. Huizenga and L. G. Moretto, Annu. Rev. Nucl. Sci. 22, 427 (1972).

[19] U. Facchini and E. Saetta-Menichella, Energ. Nucl. (Milan) 15, 54 (1968).

[20] P. M. Endt and C. Van der Leun, Nucl. Phys. A214, 1 (1973).

[21] F. Ajzenberg-Selove and T. Lauritsen, Nucl. Phys. A227, 1 (1974); F. Ajzenberg-Selove, *ibid.* A152, 1 (1970); A166, 1 (1971); A190, 1 (1972); A248, 1 (1975).

[22] T. Ericson and V. Strutinski, Nucl. Phys. 8, 284 (1958).

[23] R. A. Dayras *et al.*, Bull. Am. Phys. Soc. 23, 503 (1978).

[24] J. A. Kuehner and E. Almqvist, Phys. Rev. 134, B1229 (1964).

[25] R. Bass, Phys. Rev. Lett. 39, 265 (1977).

[26] D. Glas and U. Mosel, Nucl. Phys. A237, 429 (1975).

[27] J. V. Maher, M. W. Sachs, R. H. Siemssen, A. Weidinger, and D. A. Bromley, Phys. Rev. 188, 1665 (1969).

[28] R. M. Wieland, R. G. Stokstad, G. R. Satchler, and R. L. Rickertsen, Phys. Rev. Lett. 37, 1458 (1976).

[29] J. R. Birkelund, J. R. Huizenga, J. N. De, and D. Sperber, Phys. Rev. Lett. 40, 1123 (1978).

[30] D. Glas and U. Mosel, Phys. Lett. 18B, 9 (1978).

[31] V. Maruhn-Rezwani, K. T. R. Davies, and S. E. Koonin, Phys. Lett. 67B, 134 (1977).

[32] J. S. Blair, in *Lectures in Theoretical Physics*, edited by P. D. Kunz, D. A. Lind, and W. E. Brittin (Univ. of Colorado Press, Boulder, 1966), Vol. VIIIC, p. 375.

[33] R. Y. Cusson, *Proceedings of Heavy-Ion Collisions Falls Creek Falls, Tennessee, 1977,* edited by E. C. Halbert *et al.* (ORNL Conference Report No. 770602, Oak Ridge, Tennessee, 1977), p. 112. See also R. Y. Cusson, J. A. Maruhn, and H. W. Meldner, Phys. Rev. C 18, 2589 (1978).